



# The effect of Ce<sup>4+</sup> incorporation on structural, morphological and photocatalytic characters of ZnO nanoparticles

N. Kannadasan, N. Shanmugam<sup>\*</sup>, S. Cholan, K. Sathishkumar, G. Viruthagiri, R. Poonguzhali

Department of Physics, Annamalai University, Annamalai Nagar, Chidambaram 608 002, Tamil Nadu, India

## ARTICLE INFO

### Article history:

Received 7 July 2014

Received in revised form 23 August 2014

Accepted 26 August 2014

Available online 27 August 2014

### Keywords:

Wurtzite

X-ray photoelectron spectroscopy

Cerium

Tetavalent

Visible emission

## ABSTRACT

We report a simple chemical precipitation method for the preparation of undoped and cerium doped ZnO nanocrystals. The concentration of cerium in the products can be controlled in the range of 0.025–0.125 mol. The structure and chemical compositions of the products were characterized by X-ray diffraction, X-ray photoelectron spectroscopy; energy dispersive spectrum and Fourier transform infrared spectroscopy. The results demonstrate that Ce<sup>4+</sup> ions were successfully incorporated into the lattice position of Zn<sup>2+</sup> ions in ZnO. The morphology of the products was analyzed by field emission scanning electron microscopy and confirmed by high resolution transmission electron microscope analysis. The optical properties of the products were studied by ultraviolet–visible and room temperature photoluminescence measurements. The photoluminescence emission spectra of Ce-doped ZnO showed enhanced visible emissions as a result of 5d → 4f transition of cerium. In particular, a novel photocatalytic activity of the products was assessed using methylene blue. The obtained result reveals that Ce-doped products show higher reduction efficiency for methylene blue than the undoped ZnO.

© 2014 Elsevier Inc. All rights reserved.

## 1. Introduction

Semiconductor materials in nanodimensions have fascinated the scientific community in the recent past owing to their peculiar physical and chemical properties [1]. Among the semiconductor materials ZnO an important II–VI semiconductor material with a wide band gap of 3.37 eV and a large excitation binding energy of 60 MeV, has been studied extensively because of its potential applications in ultraviolet light-emitting diodes and laser diodes [2], field emission displays [3], solar cells [4], sensors [5,6], varistors [7], and catalysis [8]. Bhargava and Gallagher reported that doped nanocrystals of semiconductors can yield both higher luminescence efficiencies and lifetime shortening from microseconds to nanoseconds at the same time [9]. Photocatalysis is one promising approach to protecting the aquatic environment, based on its ability to oxidize low concentration of organic pollutants in water [10]. Among the different photocatalysts, ZnO has a vital role due to its high semiconducting nature. To enhance the photocatalytic efficiency, it is essential to retard the recombination of the excitons [11]. Doping is an effective way to inhibit the recombination of excitons in semiconductor photocatalyst [12]. Few earlier reports have discussed the photocatalytic activity of metal ions doped ZnO nanoparticles [13,14]. Nanoparticles of ZnO are often doped with rare earth ions such as Eu<sup>2+</sup> and Ce<sup>3+</sup> to improve their luminescent properties. It has been reported that the photocatalytic activity of semiconductor photocatalyst can be enhanced by doping rare earth ions [15] which can play a major role in the

inhibition of electron–hole recombination [16]. The change in photocatalytic activities of Ce-doped ZnO when it undergoes thermal treatments was studied in detail by Rezaei et al., who calcined the product at temperatures from 200 to 500 °C. They showed that the photocatalytic activity increases with calcination temperature up to 400 °C and then decreases [17]. Unlike their previous work [17], in the microwave assisted preparation of Ce-doped ZnO nanostructures, Rezaei et al. found the deteriorated photocatalytic activity on annealing [18]. In a report by Chi-Jung Chang et al., they showed that the photocatalytic activity of Ce-doped ZnO nanorods was reduced on too much dopant addition [19]. As per the available literature, various methods are available for the preparation of ZnO nanostructures such as sol–gel method [20], pulsed laser deposition [21], spray pyrolysis [22] and hydrothermal method [23–25]. However, many of the aforementioned methods that have been reported require more complex devices, multiple steps and a careful execution. Therefore, it is quite challenging to adopt a simple and convenient method for the preparation of semiconductor nanoparticles. Chemical precipitation method is one among the effective approaches to synthesize the ZnO nanostructures since this method is simple and cost effective. In the best of our knowledge, there is only limited report about the preparation of Ce-doped ZnO nanostructures using a simple chemical precipitation method and investigation of their photocatalytic activity with natural sunlight. Previously, we have reported the effect of Ce<sup>3+</sup> incorporation in ZnS nanocrystals [26]. In this work a simple chemical precipitation method was adopted for the preparation of ZnO and different mole percentages of cerium (Ce) doped ZnO nanocrystals. To prove cerium doped ZnO as a suitable candidate for photocatalytic application, we have evaluated the photocatalytic

<sup>\*</sup> Corresponding author.

E-mail address: [quantumgosh@rediffmail.com](mailto:quantumgosh@rediffmail.com) (N. Shanmugam).

performance of undoped and doped products by the photodegradation of methylene blue (MB) under solar-light irradiation.

## 2. Materials and Methods

All the chemicals used in this study are of AR grade with 99% purity (Merck and SD Fine Chemicals) and used without further purification. Sample preparation and dilutions were made of ultrapure water. Zinc acetate dihydrate  $[\text{Zn}(\text{CH}_3\text{COO})_2 \cdot 2\text{H}_2\text{O}]$ , cerium (III) chloride hepta hydrate  $[(\text{CeCl}_3) \cdot 7\text{H}_2\text{O}]$  and ammonium carbonate  $[(\text{NH}_4)_2\text{CO}_3]$  were used as precursors.

For the synthesis of Ce-doped ZnO, 5.49 g (0.5 mol) of zinc acetate dissolved in 50 ml of deionized water was stirred vigorously by a magnetic stirrer and cerium (III) chloride hepta hydrate with different mole percentages (0.025, 0.05, 0.075, 0.1 and 0.125 mol) prepared in 20 ml aqueous were mixed drop by drop. Then, 5.63 g (1 mol) of ammonium carbonate in 50 ml of deionized water was added drop by drop to the above mixture. The entire was stirred magnetically at 60 °C until a white precipitate was formed. The obtained dispersions were purified by dialysis against de-ionized water and ethanol several times to remove impurities [27]. The yield products were dried in a hot air oven at 100 °C for 6 h to evaporate water and organic material to the maximum extent. Finally, the product was annealed in a muffle furnace at 500 °C for 2 h. The annealed powders were pulverized to fine powders using agate mortar for further characterizations. A similar method of preparation without the addition of cerium was used to synthesize undoped ZnO nanocrystals.

For the purpose of studying the photocatalytic activity of ZnO, 0.2 g of ZnO was added to a quartz photoreactor containing 100 ml of a 1 mg/l MB aqueous solution. After stirring for 30 min in the dark in order to reach the absorption equilibrium, the mixture was irradiated with sunlight with intensity fluctuation of  $950 \pm 25 \text{ W m}^{-2}$ . The residual MB in the aqueous solution was analyzed by checking the absorbance at 664 nm in the UV–Vis absorption spectra. To determine the percentage of degradation of MB, the samples were collected at regular intervals (for every 15 min), filtered and centrifuged to remove the nanophotocatalyst particles that exist as undissolved particles in the sample and studied using UV–Vis absorption. Photodegradation studies were performed by monitoring the absorbance of the dye solution at a wavelength of 664 nm. The degradation percentage of the dye in the presence and absence of ZnO nanoparticles can be calculated from the following equation [28].

$$\%D = \frac{C_0 - C_t}{C_0} \times 100 \quad (1)$$

where  $C_0$  is the initial concentration of the dye and  $C_t$  is the concentration of dye after irradiation in selected time interval. The same procedure was adopted for cerium doped ZnO nanoparticles.

The crystalline phase and particle size of pure and Ce-doped ZnO nanoparticles were analyzed by X-ray diffraction (XRD) measurement which was carried out at room temperature by using the X'PERT-PRO diffractometer system (scan step of  $0.05^\circ$  ( $2\theta$ ), counting time of 10.16 s per data point) equipped with a Cu tube for generating Cu  $K\alpha$  radiation ( $k = 1.5406 \text{ \AA}$ ); as an incident beam in the 2-theta mode over the range of  $10^\circ$ – $80^\circ$ , operated at 40 kV and 30 mA. X-ray photoelectron spectra, arising during photoemission of electrons from the sample surface, were obtained under vacuum  $1.3 \times 10^{-7} \text{ Pa}$  at room temperature with electrostatic spectrometer HP 5950A Hewlett-Packard firm using monochromatized  $\text{AlK}_{\alpha,2}$  ( $h\nu = 1486.6 \text{ eV}$ ) X-ray excitation and the gun of low-energy electrons for compensation of electrostatic charging of samples. The spectrometer resolution measured full width at the half-maximum of  $\text{Au4f}_{7/2}$ -electron line was 0.8 eV. The values of binding energies  $E_b$  (eV) were taken relative to the binding energy of C 1s-electrons of hydrocarbonates on the sample surface, which is accepted to be equal to 285.0 eV. On the golden substrate  $E_b$  (C 1s) = 284.7 eV

and  $E_b$  ( $\text{Au4f}_{7/2}$ ) = 83.8 eV. The widths of lines  $\Gamma$  (eV), measured at half their maximum, are brought relatively to the width of C 1s-electron line of hydrocarbonates, which is accepted to be equal to 1.3 eV. The error in determination of electron binding energy values and of line widths did not exceed 0.1 eV and that of relative intensities of lines was less than 10%. The band-gap energy was measured at wavelengths in the range of 200–800 nm by UV–Vis–NIR spectrophotometer (Varian/Carry 5000) equipped with an integrating sphere and the baseline correction was performed using a calibrated reference sample of powdered barium sulfate ( $\text{BaSO}_4$ ). The photoluminescence (PL) emission spectra of the samples were recorded with a spectrofluorometer (Jobin Yvon, FLUOROLOG-FL3-11). The functional groups were determined by a SHIMADZU-8400 Fourier-transform infrared spectrometer in which the IR spectra were recorded by diluting the milled powders in KBr and the wavelength between 4000 and  $400 \text{ cm}^{-1}$  was used to assess the presence of functional groups in pure and Ce-doped ZnO. The morphological analysis was performed by a HITACHI S-4700 field emission scanning electron microscope (FESEM), and confirmed by JEOL 3010 high resolution transmission electron microscopy (HRTEM). Energy-dispersive spectrum (EDS) analysis of the products was performed during FESEM measurements. The UV–visible absorption measurements of the products during photocatalytic measurements were recorded in the wavelength range of 400–800 nm using a LAMBDA 25 PERKIN ELMER spectrometer.

## 3. Results and Discussion

The phase characteristics of the products were examined by powder X-ray diffraction. Fig. 1a shows the XRD patterns of ZnO and ZnO doped with different levels of cerium ions, respectively. All of the diffraction peaks can be indexed as wurtzite phase ZnO with lattice parameters comparable to that of the JCPDS card (36-1451). The relatively broad XRD peaks reveal the smaller size of the ZnO nanocrystals (Fig. 1b). It is noticed that for a lower concentration of Ce-doping no other crystalline impurities were detected by XRD, suggesting that the doping limit of Ce in ZnO matrix is  $\geq 0.075$  mol. However, on higher levels of Ce-doping (0.1 and 0.125 mol), a small peak positioned at  $2\theta = 28.6^\circ$  related to (111) reflection plane of  $\text{CeO}_2$  is noted [29]. Similar behavior was reported by Faisal et al. on higher concentration of cerium doped ZnO nanocrystals [30].

The average crystalline sizes of the synthesized samples were calculated using the Debye–Scherer formula [26]

$$D = \frac{0.9\lambda}{\beta \cos \theta} \quad (2)$$

where  $\lambda$  is the wavelength for the  $K\alpha$  component of the employed copper radiation (1.54056 Å),  $\beta$  is the corrected full width at half maximum (FWHM) and  $\theta$  is the Bragg's angle. The lattice constants  $a$  and  $c$  were calculated using the following formula used for hexagonal systems [31]:

$$\frac{1}{d^2} = \frac{4}{3} \left( \frac{h^2 + hk + k^2}{a^2} \right) + \frac{l^2}{c^2} \quad (3)$$

where  $d$  is the lattice spacing,  $a$  and  $c$  are the lattice constants,  $h$ ,  $k$ , and  $l$  are the miller indices,  $\theta$  is the angle of corresponding peak and  $\lambda$  is the wavelength of X-ray used (1.5406 Å). The unit cell volume of the products is given by the formula  $V = (0.866) a^2 c$  [32].

The results of the calculation of particle size, unit-cell parameters and unit-cell volume are given in Table 1. As shown in the table the lattice parameters of cerium doped ZnO are found to be slightly larger than those of pure ZnO for all the concentration of doping. This is due to larger ionic radius of  $\text{Ce}^{4+}$  (1.01 Å) than that of  $\text{Zn}^{2+}$  (0.74 Å) [33]. From Table 1, it can be observed that the average grain size of ZnO is around 24 nm. After doping with cerium, the grain size reduced to 15, 16, 11,

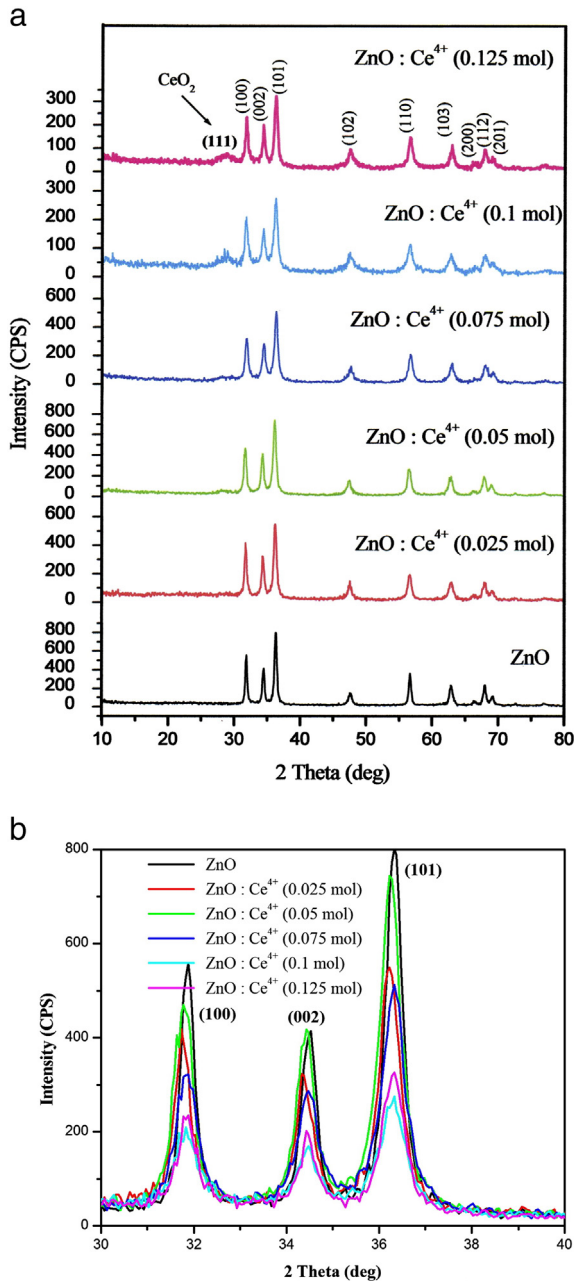


**Fig. 1.** (a) X-ray diffraction patterns of pure and Ce<sup>4+</sup> doped ZnO nanoparticles. (b) X-ray diffraction patterns of pure and Ce<sup>4+</sup> doped ZnO nanoparticles enlarged view of (100), (002) and (101) peaks.

8 and 11 nm respectively, for the samples doped with 0.025, 0.05, 0.075, 0.1 and 0.125 mol of cerium. However, the estimated sizes of CeO<sub>2</sub> are 3 and 2.75 nm respectively, for 0.1 and 0.125 mol of Ce-doping. The values

**Table 1**  
XRD derived parameters of undoped and Ce<sup>4+</sup> doped ZnO nanoparticles.

Samples	Particle size (nm)	Lattice parameters (Å)			Volume (Å <sup>3</sup> )
		a = b	c	c/a	
ZnO	24	3.242	5.204	1.604	47.570
ZnO:Ce <sup>4+</sup> (0.025 M)	15	3.254	5.216	1.602	47.828
ZnO:Ce <sup>4+</sup> (0.05 M)	16	3.251	5.214	1.603	47.722
ZnO:Ce <sup>4+</sup> (0.075 M)	11	3.244	5.205	1.604	47.435
ZnO:Ce <sup>4+</sup> (0.1 M)	8	3.243	5.208	1.605	47.491
ZnO:Ce <sup>4+</sup> (0.125 M)	11	3.243	5.206	1.605	47.415

of variation of aspect ratio (*c/a*) are almost the same for all the concentration of doping and the change is noted only in the third decimal. Moreover, the obtained *c/a* values in the present study are in good correlation with the standard value of 1.60 for ZnO. This suggests that the larger Ce<sup>4+</sup> is able to substitute the smaller Zn<sup>2+</sup> ions in the matrix with little or no effect on the overall crystal structure. We also predict from the data in Table 1 that there is about a 0.166% decrease in the specific volume as the particle size decreases from about 24 to 8 nm. This could be explained by the fact that as the particle sizes increase, the effect of the surface forces on the bulk becomes progressively less.

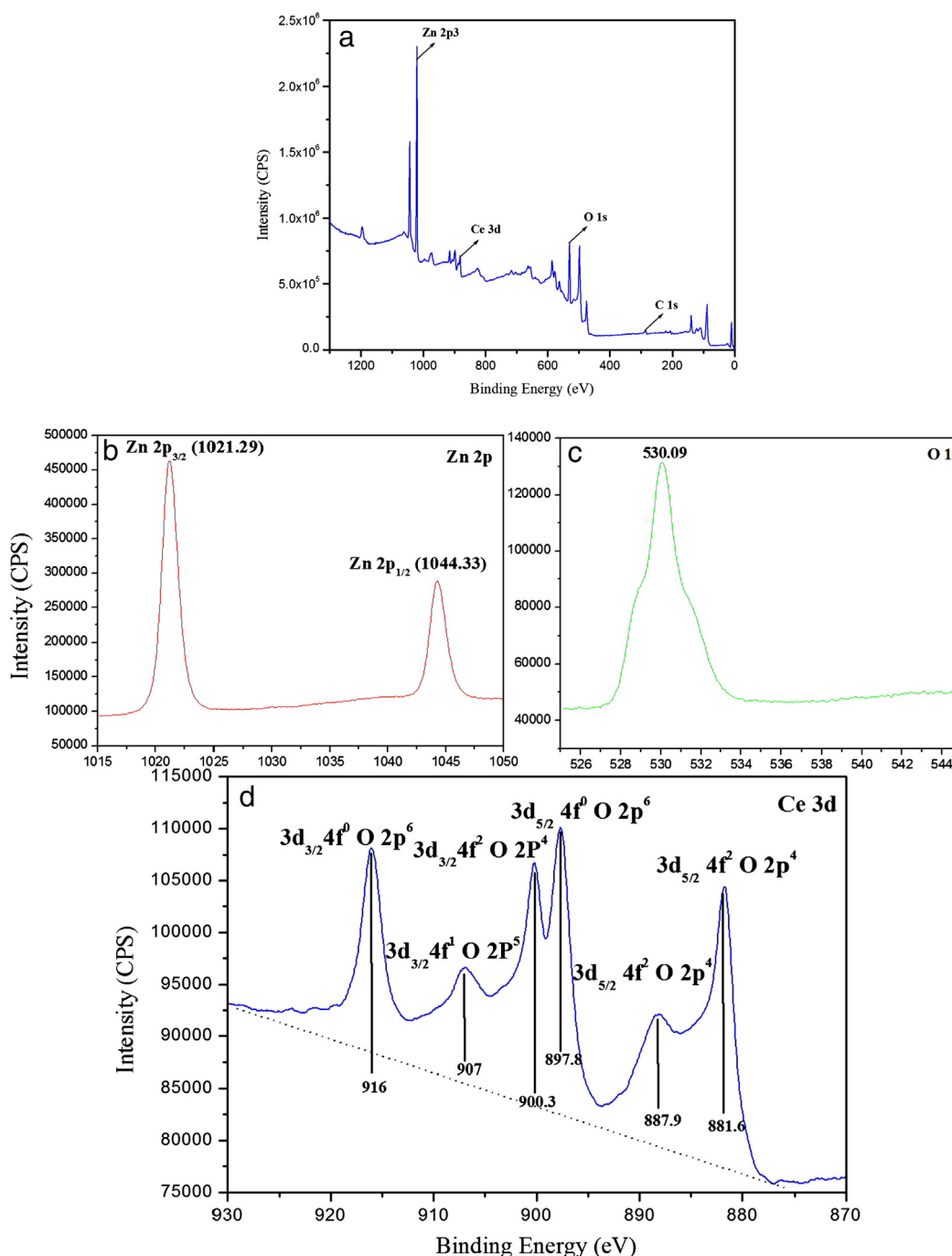
It is a known fact that there are two different oxidation states for the element cerium. However, the Ce<sup>4+</sup> oxidation state is very stable compared with Ce<sup>3+</sup> oxidation state. To ascertain the valence of incorporating cerium into the lattice position of Zn<sup>2+</sup>, XPS was recorded. Fig. 2a shows the XPS result of 0.075 mol Ce-doped ZnO. The high resolution scan results of Ce 3d, Zn 2p and O 1s are given in Fig. 2b–d. By considering the carbon C 1s peak (285 eV) as reference, the binding energy calibration of XPS has been made. As shown in Fig. 2b, the peaks positioned at 1021.29 and 1044.33 eV are assigned to Zn 2p<sub>3/2</sub> and Zn 2p<sub>1/2</sub>, respectively. From Fig. 2c, we can intercept that the O 1s peak at 530 eV can be assigned to lattice oxygen in ZnO [34]. In the Ce 3d spectrum (Fig. 2d), three spin orbital doublets are identified and are in good agreement with earlier reports [35–37]. The binding energy of Ce 3d<sub>3/2</sub> is seen at 900.3, 907 and 916 eV, whereas, for Ce 3d<sub>5/2</sub>, it is located at 881.6, 887.9 and 897.8 eV. These binding energies are noticed as characteristic peaks of tetravalent Ce. No peaks related to Ce<sup>3+</sup> are noted, confirming that the incorporated cerium is in the form of Ce<sup>4+</sup> [38]. The mechanism behind the formation of three doublets with the configuration 3d 4f<sup>0</sup>, 3d 4f<sup>1</sup> (L) and 3d 4f<sup>2</sup> (L)<sup>2</sup> is explained in the following manner. In the ground state the O 2p valence band is completely occupied, but the Ce<sup>4+</sup> level is most probably empty. The Ce 4f level is positioned near the top of the oxygen 2p valence band, therefore 4f<sup>0</sup> configuration is strongly mixed with the charge transfer state 4f<sup>1</sup> (L) where L denotes a hole in the O 2p valence band. This leads to a weak hybridization between the valence band and the 4f state. In the final state of XPS, a 3d core electron is removed and the 4f level is pulled down as a result of attractive force known as core hole potential. This causes charge transfer of oxygen 2p to Ce 4f states. This is the potential reason for obtaining three doublets [39–42]. The composition analysis of XPS revealed that the content of Ce<sup>4+</sup> in ZnO is 3.8 at.% which is in good agreement with the EDX result.

Fig. 3a shows the UV–Vis reflectance spectra of undoped and Ce-doped ZnO samples. All the products exhibit good optical quality in the visible region since the complete reflectance in the 428–441 nm range. As the concentration of Ce-doping increases, the absorption edges are blue shifted with an intensity reduction in the reflectance due to quantum confinement effect. For the purpose of obtaining band gap values of ZnO and Ce-doped ZnO the well-known Eq. (1) was used.

$$\alpha = \frac{A(h\nu - E_g)^{1/2}}{h\nu} \rightarrow \quad (4)$$

where  $\alpha$ ,  $E_g$  and  $A$  are the absorption coefficient, band gap, and constant, respectively. By extrapolating the linear region in the plots of  $(\alpha h\nu)^2$  versus  $h\nu$  (Fig. 3b), the band gap of ZnO is found to be 3.4 eV, whereas the values of ZnO doped with 0.025, 0.05, 0.075, 0.1 and 0.125 mol of cerium are about 3.48, 3.53, 3.67, 3.76 and 3.65 eV respectively.

It is clear that the optical band gaps of these samples increase with the increase of Ce-dopants inside the host matrix up to 0.1 mol followed by a decrease in its value. The highest band gap of 3.76 eV witnessed on 0.1 mol of cerium incorporation can be attributed to Burstein–Moss effect [43]. It is noted that the  $E_g$  value of 0.125 mol Ce-doped sample is decreasing drastically when compared to that of 0.1 mol Ce-doped ZnO sample. This is due to the contribution of secondary phase, CeO<sub>2</sub>. As seen in Fig. 1a, the intensity level of CeO<sub>2</sub> in 0.125 mol of Ce-doped ZnO is higher than that of the doping concentration of 0.1 mol.



**Fig. 2.** (a) Surface scan XPS spectra of the  $\text{Ce}^{4+}$  (0.075 mol)-doped ZnO nanoparticles. (b–d) XPS spectra of  $\text{Ce}^{4+}$  (0.075 mol) doped ZnO nanoparticles.

Furthermore, the obtained  $E_g$  value for 0.125 mol of Ce-doped sample is close to the  $E_g$  value of  $\text{CeO}_2$  (3.71 eV) [44] and this confirms that the secondary phase is an effective parameter in shifting of the band gap of the Ce-doped ZnO samples. Aydin et al. have reported the same type of secondary phase effect on the band gap of Fe-doped CdO nanocrystals [45].

The PL properties of as-prepared ZnO and Ce-doped ZnO nanocrystals were studied at room temperature (Fig. 4). A sharp UV peak at 400 nm in wavelength, accompanied by four weaker visible peaks at ~445, 467, 480 and 525 nm in wavelength was observed when ZnO was excited with a wavelength of 325 nm. The sharp UV emission can be ascribed to the near-band-edge emission of ZnO originating from electron–hole recombination [46–48]. The appearance of the emission band at 445 nm is attributed to the transition from Zn

interstitial to valence band, whereas blue emission at 467 and 480 nm and green emission at 527 nm are most probably from the oxygen vacancies. The similar emission behavior of ZnO has been reported by Qingzhi Wu et al. [49]. On doping with Ce, with an increase in Ce content we predict that the band gap structure of ZnO nanocrystals can be tailored and new emission centers are generated, which leads to the intensity quenching of UV emission and enhancement in the visible emissions. In comparison to the pure ZnO, the peak position of UV emission remains unaffected with cerium doping while visible emission bands are slightly red shifted. The possible mechanism behind the quenching of UV emission and enhancement of visible emissions is explained as follows. For Ce-doped samples, with the increase in Ce content, the intensity of UV band is found to decrease as a result of the inhibition of recombination of the excitons. It is a well known fact that conduction



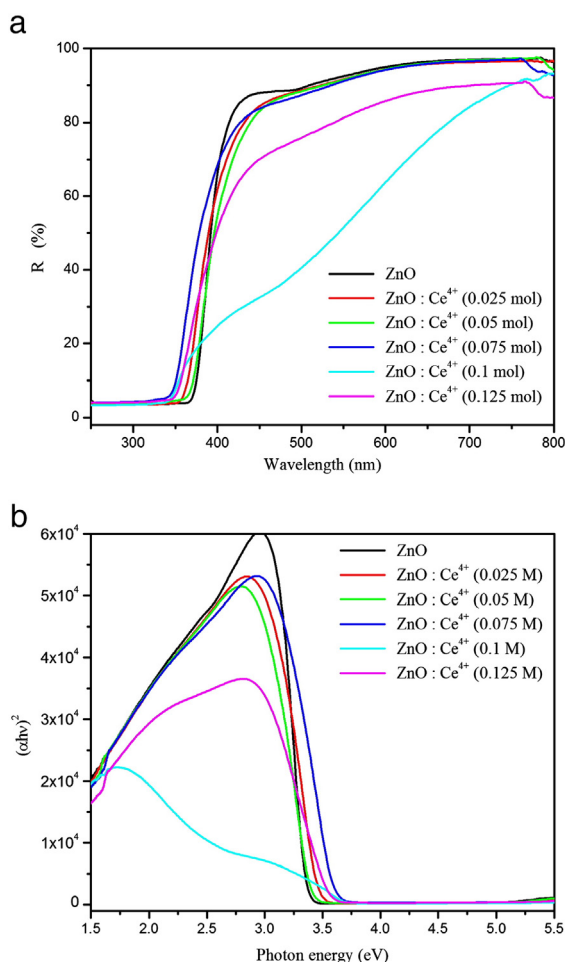


**Fig. 3.** (a) UV-Vis-diffuse reflectance spectra of pure and  $\text{Ce}^{4+}$  doped ZnO nanoparticles. (b) Plot of direct band gap energy for pure and  $\text{Ce}^{4+}$  doped ZnO nanoparticles.

and valence bands refer to the reduced and oxidized states in the semiconductor.

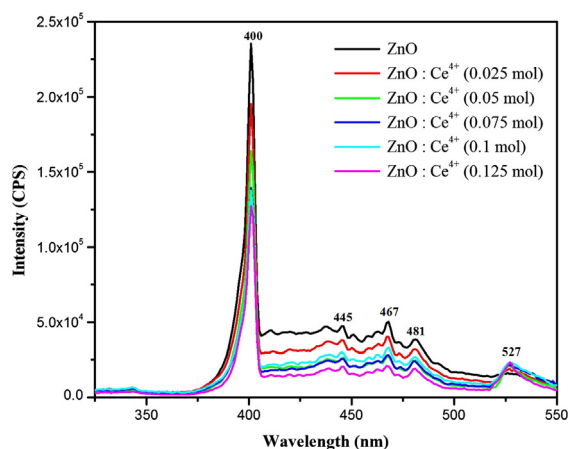
When an amount of energy greater than the band gap energy is supplied from excitation energy to one of the electrons in the valence band, it will make a quantum jump to the conduction band thereby creating a hole in the valence band. The whole process may be therefore described as the disappearance of a quantum of energy supplied with the creating of a pair of observable particles. In ZnO the conduction band electrons are related to the reduced form of  $\text{Zn}^{2+}$  (i.e.  $\text{Zn}^+$ ) and the valence

band holes refer the oxidized form of  $\text{O}^{2-}$  (i.e.,  $\text{O}^-$ ). The band gap excitation is the photoexcitation of an electron from  $\text{O}^{2-}$  to  $\text{Zn}^{2+}$  and the reversion of the electron from  $\text{Zn}^+$  to  $\text{O}^-$  leads to pair annihilation. The low near band gap photoluminescence of Ce-doped ZnO reveals better inhibition of pair annihilation and resulted in UV quenching. Now part of the electrons in the conduction band may be utilized to convert  $\text{Ce}^{4+}$  ions into  $\text{Ce}^{3+}$  ions which are more stable than  $\text{Zn}^+$  [50]. Further, the energy of the excited electrons in the conduction band of the ZnO is transferred to the newly created  $\text{Ce}^{3+}$  ions and leading to  $5d \rightarrow 4f$  transition which may account for intense visible emissions [51].

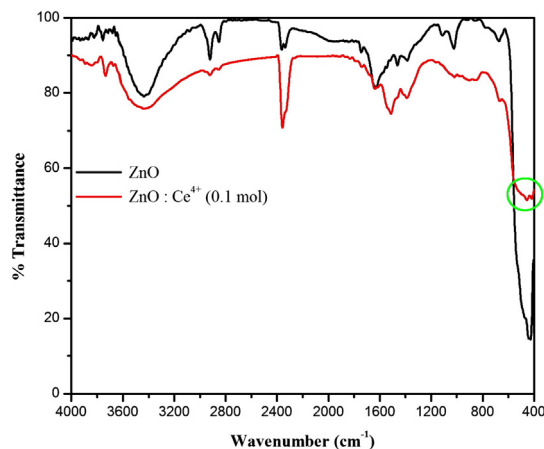
The FT-IR spectra of the as prepared ZnO and 0.1 mol of cerium doped ZnO are shown in Fig. 5. The spectra of ZnO and  $\text{ZnO}:\text{Ce}^{4+}$  are quite different. Clearly, the IR spectrum of ZnO exhibits sharp peaks at 3433 and 1630  $\text{cm}^{-1}$  respectively corresponding to stretching and bending vibrations of the OH group of atmospheric water on the ZnO surface, while the Zn–O peak is presented at 434  $\text{cm}^{-1}$  [52]. It is a well-known fact that nanoparticles of ZnO with sizes in the range of 20 nm can show a broad IR band around 430  $\text{cm}^{-1}$  [53]. This is true in the present case also since the size of ZnO estimated from the XRD analysis is around 24 nm. The absorption band corresponding to 2360  $\text{cm}^{-1}$  is assigned for the existence of  $\text{CO}_2$  molecules in air. Other peaks at 1021 and 667  $\text{cm}^{-1}$  show the presence of  $\text{CH}_3$  groups. Compared with undoped ZnO, the IR spectrum of Ce-doped ZnO indicates the presence of broad –OH stretching band at 3446  $\text{cm}^{-1}$  revealing the increased water absorption capability of cerium. The spectrum of Ce-doped sample additionally has peaks at 1388, 454 and 415  $\text{cm}^{-1}$ , which respectively match with the C–O stretching complexed with zinc, ZnO bending vibration and  $\text{CeO}_2$  formation.

Fig. 6(a, b) depicts the FESEM images of the undoped and Ce-doped ZnO samples. Fig. 6a demonstrates that the ZnO yields large number of pseudo spherical particles and a few of them are showing hexagonal wurtzite phase of ZnO, with diameter of ~40–50 nm. In Fig. 6c, it can be observed that by doping with cerium, ZnO exhibits aggregates of nearly spherical morphology. The EDX analysis is used to determine the local chemical composition of our samples. A typical EDX spectra of pure and doped ZnO are shown in Fig. 6(b, d), which are exhibiting the presence of zinc (Zn), and oxygen (O). Together with Zn and O, the existence of cerium (Ce) in the EDX pattern of  $\text{ZnO}:\text{Ce}$  indicates the successful doping of cerium in the ZnO matrix.

In order to gain deep insight into the mechanisms of the phase and morphological transformation, HRTEM analysis was performed. The HRTEM image of the ZnO is shown in Fig. 7a. The images of the individual nanocrystallites which depict the well-resolved lattice planes correspond to (101) plane of wurtzite ZnO. The close proximity of the nanocrystallites seen in the image suggested a compact arrangement of the individual crystallites. Fig. 7d shows the HRTEM image of Ce-doped ZnO. It is noted that the structural components are identical



**Fig. 4.** PL emission spectra of pure and  $\text{Ce}^{4+}$  doped ZnO nanoparticles.



**Fig. 5.** FT-IR spectra of pure and  $\text{Ce}^{4+}$  (0.1 mol) doped ZnO nanoparticles.

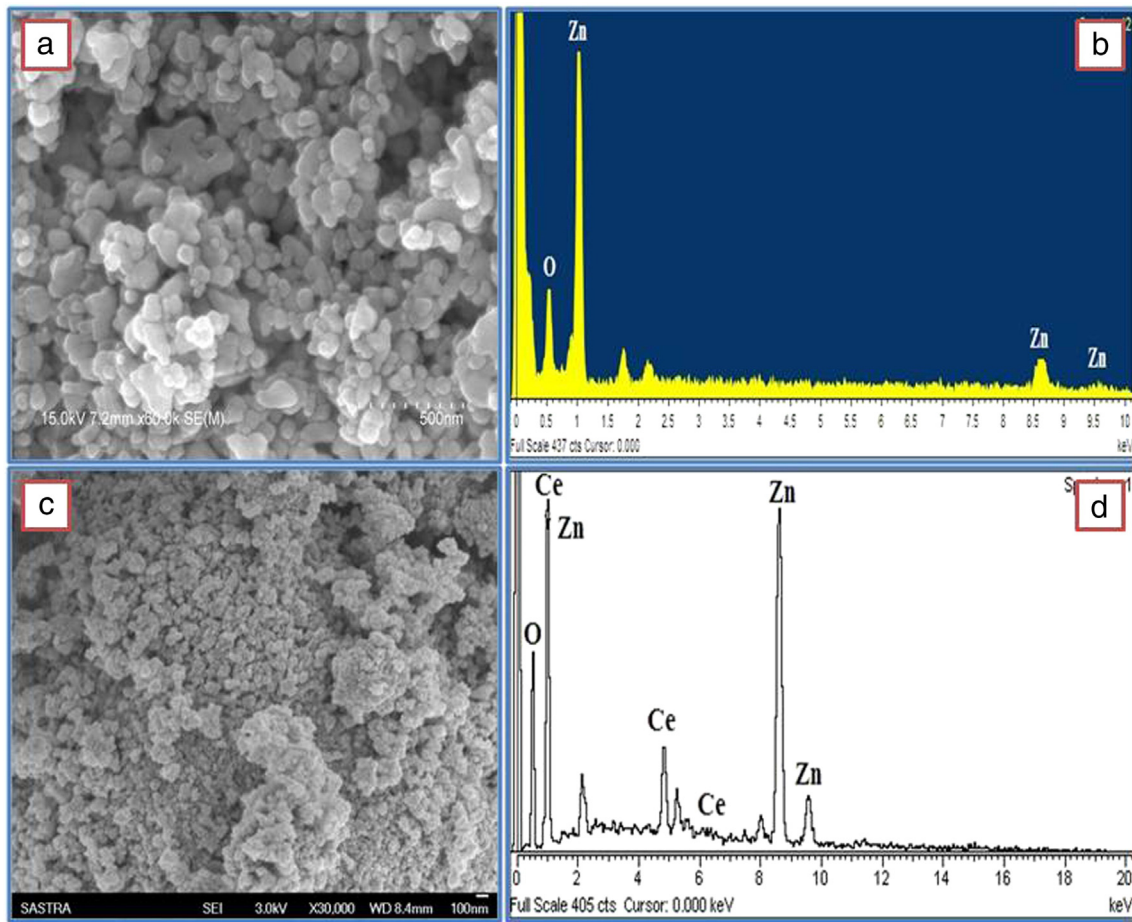


Fig. 6. FESEM images of pure (a) and  $\text{Ce}^{4+}$  (0.075 mol) doped (c) ZnO nanostructures corresponding EDX spectra (b, d).

with undoped ZnO and no apparent dislocation and other obvious crystal defects are seen. Transmission electron microscopy (TEM) measurements (Fig. 7a, e) confirm the morphology of ZnO with and without cerium. The TEM measurements of ZnO clearly show pseudo spherical particles having a size variation between 25 and 40 nm (Fig. 7b), while for cerium doped ZnO they show spherical and hexagonal morphology with sizes in the range of 10–40 nm (Fig. 7e). The SAED patterns of ZnO and  $\text{ZnO}:\text{Ce}^{4+}$  are shown in Fig. 7(c, f). The SAED pattern of ZnO phase exhibits the well defined electron diffraction spots, confirming the single crystalline nature of the hexagonal phase of ZnO nanocrystals (Fig. 7c). On the other hand, SAED pattern of  $\text{ZnO}:\text{Ce}^{4+}$  shows circular rings corresponding to diffraction planes of ZnO (Fig. 7f).

The photocatalytic activity is based on the reactive nature of an electron–hole pair generated in semiconductor nanoparticles. Under illumination by light of energy greater than the semiconductor band gap electron is excited to the conduction band and electron in the conduction band migrates to the particle surface. If no recombination takes place, these charge carriers can react with adsorbed molecules, e.g. with water, hydroxyl anion, oxygen or organic compounds. To explore the potential application of ZnO nanoparticles as a photocatalyst, degradation experiment of methylene blue (MB) was carried out. The absorption peak of MB centered at 664 nm is monitored to characterize the degradation effect. The change in the absorption spectra of MB solution with different irradiation intervals over the ZnO photocatalyst is illustrated in Fig. 8. From the figure, it is clear that by increasing the irradiation time the maximum absorption peak decreases. This indicates that the concentration of dye decreases in the presence of ZnO NPs under solar light illumination. The decrease in the absorption of the solution was due to the destruction of the homo and hetero-polyaromatic rings present in the dye molecules or due to rapid degradation of MB,

which is confirmed by the disappearance of the absorbance peak of methylene blue. The possible mechanism is given by the following equations



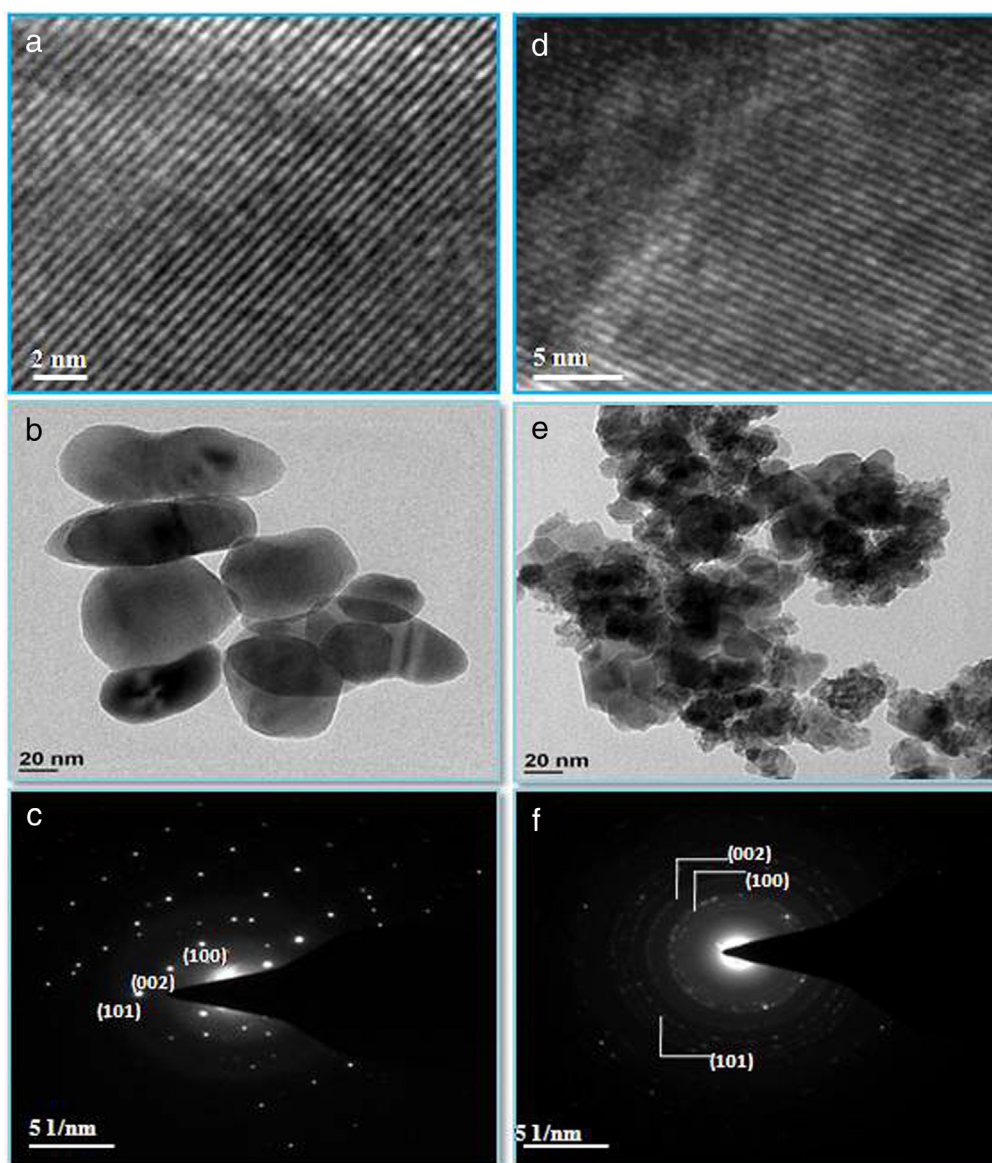


Fig. 7. HRTEM micrographs of undoped (a) and Ce<sup>4+</sup> (0.075 mol) doped (d) ZnO nanocrystals, corresponding TEM images (b, e) and corresponding SAED patterns (c, f).

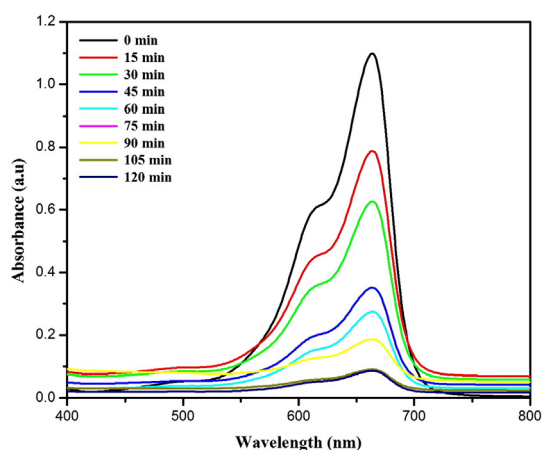
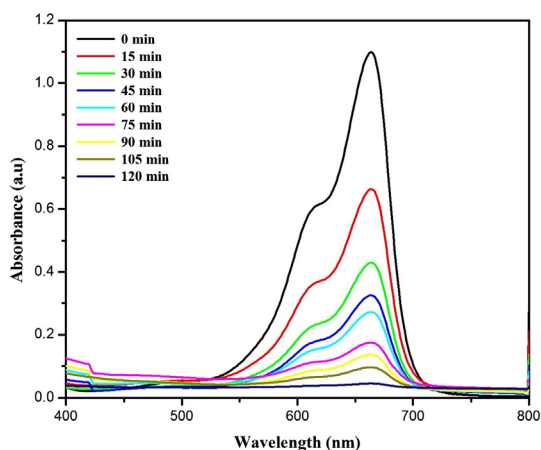


Fig. 8. Time dependent UV-Vis absorption spectra of the photocatalytic degradation of MB in the presence of ZnO nanoparticles.

The photocatalytic degradation of MB in aqueous solution was initiated by solar light irradiation to excite an electron from the valence band (VB) to the conduction band (CB) of the ZnO nanoparticles resulting in the formation of photogenerated electron hole pairs. The highly oxidative holes on VB not only directly decompose the dye molecule absorbed on the surface of ZnO nanoparticles, but also oxidize H<sub>2</sub>O or OH<sup>-</sup> to form OH<sup>•</sup> with high activity and indirectly degrade the dye molecules in the aqueous solution. In addition, the electron may then react with species absorbed at the surface, yielding radicals such as O<sub>2</sub><sup>-</sup> as a result of the presence of hydroxyl groups, water and oxygen at the surface of the ZnO nanoparticles. These radicals then react with the surrounding organic dye molecules, leading to volatile degradation by-products or entire mineralization into CO<sub>2</sub>, H<sub>2</sub>O and mineral acids. Fig. 9 exhibits the variation in absorption spectra of MB under solar light exposure at different time intervals in the presence of 0.075 mol of Ce-doped ZnO. It is noted from the figure, Ce<sup>4+</sup> incorporated ZnO exhibits higher photocatalytic performance than that of undoped product. Mechanism behind the photocatalytic activity of Ce-doped ZnO is explained below. It is a known fact that Ce<sup>4+</sup> ions after incorporation into the ZnO matrix absorb photoexcited electrons and changed into





**Fig. 9.** Time dependent UV-Vis absorption spectra of the photocatalytic degradation of MB in the presence of cerium (0.075 mol) doped ZnO nanoparticles.

$\text{Ce}^{3+}$  ions. These  $\text{Ce}^{3+}$  ions react with  $\text{O}_2$  molecule and produce the radical  $\text{O}_2^{\cdot-}$  and  $\text{Ce}^{4+}$  ions (Scheme 1).



In this way, by continuous trapping of photogenerated electrons,  $\text{Ce}^{4+}$  ions inhibit the electron-hole recombination. This means that  $\text{Ce}^{4+}$  on the surface of ZnO NPs may act as an electron scavenger. In addition, Ce-doped ZnO NPs have wide band gap energy than that of pure ZnO due to their smaller particle size, which can lead to extended electron-hole stability and favor photocatalytic degradation efficiency.

The photocatalytic efficiency of catalysts was evaluated in terms of percentage of dye degrade using Eq. (1). The calculated values are listed in Table 2. From the table it is noted that the degradation efficiency of Ce-doped ZnO is greater than that of undoped products after 120 min illumination. Plots of percentage of degradation of MB in the presence

**Table 2**

The effect of MB dye degradation by undoped, cerium (0.075 M) doped ZnO nanocrystals.

Time (min)	% degradation of MB dye	
	ZnO	ZnO: $\text{Ce}^{4+}$ (0.075 M)
0	0	0
15	17.43	48.44
30	40.2	61.46
45	58.63	64.22
60	59.55	75.22
75	73.22	82.4
90	74.14	84.07
105	76.06	89.74
120	78.65	94.33

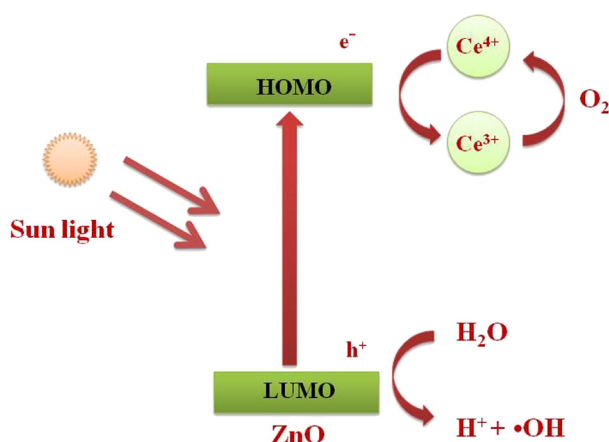
of different catalysts as a function of irradiation time are presented in Fig. 10. It is evident that the degradation of MB is faster with cerium doped ZnO nanocrystals than that of undoped ZnO subjected to analysis. For Ce-doped ZnO almost 61.46% of degradation was observed at 30 min. Also the rate constant values for dye degradation for the catalysts were calculated using first order rate equation

$$\ln \frac{C_0}{C_t} = kt \quad (17)$$

where,  $k$  is the first order rate constant. Fig. 11 shows the plot depicting a linear relationship between  $\ln \frac{C_0}{C_t}$  and time for all the samples and from the slope of the graph, rate constant values were calculated. The rate constant value for undoped ZnO was found to be  $0.01312 \text{ min}^{-1}$ , while for Ce (0.075 mol) doped sample, it was increased to  $0.02281 \text{ min}^{-1}$ . The increased  $k$  value of Ce-doped ZnO suggests the excellent photocatalytic activity of ZnO on cerium doping. Faisal et al. studied the degradation efficiency of Ce-doped ZnO nanorods against methylene blue. They also concluded that the doping of cerium showed better photocatalytic degradation of MB than the pure ZnO [30].

#### 4. Conclusion

In conclusion, the results illustrate that the simple chemical precipitation method provides a facile and efficient route to specifically prepare undoped and cerium doped ZnO nanocrystals. The hexagonal wurtzite structure of ZnO remains stable even after higher concentration of cerium doping creating a secondary phase. The results of XPS



**Scheme 1.** Illustration of photodegradation mechanism of MB over  $\text{Ce}^{4+}$ -doped ZnO photocatalysts.

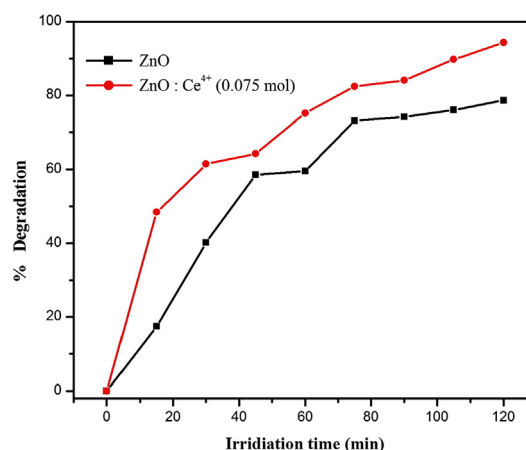


**Fig. 10.** The effect of MB dye degradation by undoped and cerium (0.075 mol) doped ZnO nanoparticles.



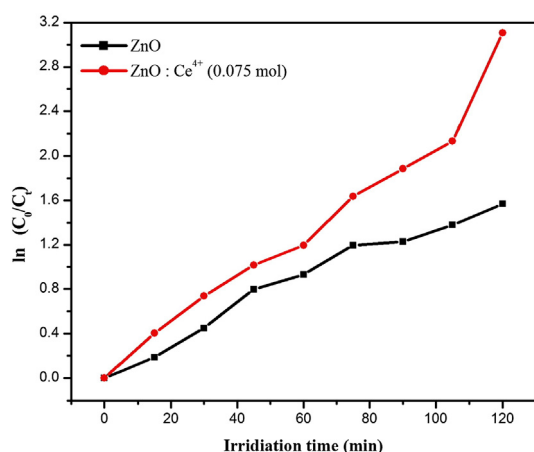


**Fig. 11.** Kinetic study of photodegradation of MB in the presence of undoped and cerium (0.075 mol) doped ZnO nanoparticles.

confirmed that the doped cerium ions are in tetravalence. The PL results of doped ZnO exhibit enhanced visible emissions due to the  $5d \rightarrow 4f$  transition of cerium. Photocatalytic experiments showed that doped ZnO decolorizes methylene blue faster than undoped ZnO. The development of such photocatalysts in large scale may open up a new path to address water contamination and environmental pollution.

## Acknowledgments

The authors wish to thank Dr. S. Barathan, professor and head, Department of Physics, Annamalai University, for providing necessary facilities to carry out this work. Authors cordially thank Dr. N. Krishnakumar, assistant professor, Annamalai University, for his stimulating discussions during the performance of this work.

## References

- [1] S.N. Das, J.P. Kar, J.H. Choi, T.I. Lee, K.J. Moon, J.M. Myoung, Fabrication and characterization of ZnO single nanowire-based hydrogen sensor, *J. Phys. Chem. C* 114 (2010) 1689.
- [2] M.H. Huang, S. Mao, H. Feick, H. Yan, Y. Wu, H. Kind, E. Weber, R. Russo, P. Yang, Room-temperature ultraviolet nanowire nanolasers, *Science* 292 (2001) 1897.
- [3] Z.S. Wang, C.H. Huang, Y.Y. Huang, Y.J. Hou, P.H. Xie, B.W. Zhang, H.M. Cheng, A highly efficient solar cell made from a dye-modified ZnO-covered TiO<sub>2</sub> nanoporous electrode, *Chem. Mater.* 13 (2001) 678.
- [4] Z. Liu, C. Liu, J. Ya, E. Lei, Controlled synthesis of ZnO and TiO<sub>2</sub> nanotubes by chemical method and their application in dye-sensitized solar cells, *Renew. Energy* 36 (2011) 1177.
- [5] C.J. Lee, T.J. Lee, S.C. Lyu, Y. Zhang, H. Ruh, H.J. Lee, Field emission from well-aligned zinc oxide nanowires grown at low temperature, *Appl. Phys. Lett.* 81 (2002) 3648.
- [6] D. Sridevi, K.V. Rajendran, Synthesis and optical characteristics of ZnO nanocrystals, *Bull. Mater. Sci.* 32 (2009) 165.
- [7] I. Honma, S. Hirakawa, K. Yamada, J.M. Bae, Synthesis of organic/inorganic nanocomposites protonic conducting membrane through sol-gel processes, *Solid State Ionics* 118 (1999) 29.
- [8] J.H. Zeng, B.B. Jin, Y.F. Wang, Facet enhanced photocatalytic effect with uniform single-crystalline zinc oxide nanodisks, *Chem. Phys. Lett.* 472 (2009) 90.
- [9] R.N. Bhargava, D. Gallagher, X. Hong, A. Nurmikko, Optical properties of manganese-doped nanocrystals of ZnS, *Phys. Rev. Lett.* 72 (1994) 416.
- [10] D. Ravelli, D. Dondi, M. Fagnoni, A. Albini, Photocatalysis. A multi-faceted concept for green chemistry, *Chem. Soc. Rev.* 38 (7) (2009) 1999–2011.
- [11] F. Dong, H.Q. Wang, Z.B. Wu, J.F. Qiu, Marked enhancement of photocatalytic activity and photochemical stability of N-doped TiO<sub>2</sub> nanocrystals by Fe<sup>3+</sup>/Fe<sup>2+</sup> surface modification, *J. Colloid Interface Sci.* 343 (2010) 200–208.
- [12] C.M. The, A.R. Mohamed, Roles of titanium dioxide and ion-doped titanium dioxide on photocatalytic degradation of organic pollutants (phenolic compounds and dyes) in aqueous solutions: a review, *J. Alloys Compd.* 509 (2011) 1648–1660.
- [13] Japinder Kaur, Sonal Singhal, Facile synthesis of ZnO and transition metal doped ZnO nanoparticles for the photocatalytic degradation of methyl orange, *Ceram. Int.* 40 (2014) 7417–7424.
- [14] Manjula G. Nair, M. Nirmala, K. Rekha, A. Anukalini, Structural, optical, photocatalytic and antibacterial activity of ZnO and Co doped ZnO nanoparticles, *Mater. Lett.* 65 (2011) 1797–1800.
- [15] T.M. Williams, D. Hunter, A.K. Pradhan, Photoinduced piezo-optical effect in Er doped ZnO films, *Appl. Phys. Lett.* 89 (2006) 043116–043119.
- [16] C.-H. Wu, J.-M. Chern, Kinetics of photocatalytic decomposition of methylene blue, *Ind. Eng. Chem. Res.* 45 (2006) 6450–6457.
- [17] M. Rezaei, A. Habibi-Yangjeh, Simple and large scale refluxing method for preparation of Ce-doped ZnO nanostructures as highly efficient photocatalyst, *Appl. Surf. Sci.* 265 (2013) 591–596.
- [18] M. Rezaei, A. Habibi-Yangjeh, Microwave-assisted preparation of Ce-doped ZnO nanostructures as an efficient photocatalyst, *Mater. Lett.* 110 (2013) 53–56.
- [19] Chi-Jung Chang, Chang-Yi Lin, Mu-Hsiang Hsu, Enhanced photocatalytic activity of Ce-doped ZnO nanorods under UV and visible light, *J. Taiwan Inst. Chem. Eng.* 45 (2014) 1954–1963.
- [20] Z. Pan, X. Tian, S. Wu, X. Yu, Z. Li, J. Deng, C. Xiao, G. Hu, Z. Wei, Investigation of structural, optical and electronic properties in Al–Sn co-doped ZnO thin films, *Appl. Surf. Sci.* 265 (2013) 870.
- [21] Y.R. Ryu, W.J. Kim, H.W. White, Fabrication of homostructural ZnO p–n junctions, *J. Cryst. Growth* 219 (2000) 419.
- [22] S.M. Rozati, S. Akeste, Influence of substrate temperature on the structure of ZnO:Al thin films, *Cryst. Res. Technol.* 43 (3) (2008) 273.
- [23] S. Ameen, M.S. Akhter, H.-K. Seo, Y.S. Kim, H.S. Shin, Influence of Sn doping on ZnO nanostructures from nanoparticles to spindle shape and their photoelectrochemical properties for dye sensitized solar cells, *Chem. Eng. J.* 187 (2012) 351.
- [24] N. Kiomarsipour, R. Shojazadeh, Hydrothermal synthesis and optical property of scale and spindle-like ZnO, *Ceram. Int.* 39 (2013) 813.
- [25] R. Shi, P. Yang, X. Dong, Q. Ma, A. Zhang, Growth of flower-like ZnO on ZnO nanorod arrays created on zinc substrate through low-temperature hydrothermal synthesis, *Appl. Surf. Sci.* 264 (2013) 162.
- [26] N. Shanmugam, S. Cholan, N. Kannadasan, K. Sathishkumar, G. Viruthagiri, Luminance behavior of Ce<sup>3+</sup> doped ZnS nanostructures, *Spectrochim. Acta A* 118 (2014) 557.
- [27] V. Ramasamy, C. Anandan, G. Murugadoss, Structural, morphological and photoluminescence studies of multi shells coated ZnO nanocomposites, *Superlattice. Microsc.* 61 (2013) 106–114.
- [28] H.R. Pourtehdar, A. Norozi, M.H. Keshavarz, A. Semnani, Nanoparticles of zinc sulfide doped with manganese, nickel and copper as nanophotocatalyst in the degradation of organic dyes, *J. Hazard. Mater.* 162 (2008) 674.
- [29] M. Yousefi, M. Amiri, R. Azimrad, A.Z. Moshfegh, Enhanced photoelectrochemical activity of Ce doped ZnO nanocomposite thin films under visible light, *J. Electroanal. Chem.* 661 (2011) 106.
- [30] M. Faisal, Adel A. Ismail, Ahmed A. Ibrahim, Houcine Bouzid, Saleh A. Al-Sayari, Highly efficient photocatalyst based on Ce doped ZnO nanorods: controllable synthesis and enhanced photocatalytic activity, *Chem. Eng. J.* 229 (2013) 225–233.
- [31] Oleg Lupina, Lee Chowa, Guangyu Chaic, Beatriz Roldana, Ahmed Naitabdia, Alfons Schultea, Helge Heinricha, Nanofabrication and characterization of ZnO nanorod arrays and branched microrods by aqueous solution route and rapid thermal processing, *Mater. Sci. Eng. B* 145 (2007) 57–66.
- [32] P. Dhamodharan, R. Gobi, N. Shanmugam, N. Kannadasan, R. Poonguzhali, S. Ramya, Synthesis and characterization of surfactants assisted Cu<sup>2+</sup> doped ZnO nanocrystals, *Spectrochim. Acta A Mol. Biomol. Spectrosc.* 131 (2014) 125–131.
- [33] Javed Iabal, Xiaofang Liu, Huichao Zhu, Chongchao Pan, Yong Zhang, Dapeng Yu, Ronghai Yu, Trapping of Ce electrons in band gap and room temperature ferromagnetism of Ce<sup>4+</sup> doped ZnO nanowires, *J. Appl. Phys.* 106 (2009) 083515.
- [34] Jihui Lang, Qiang Han, Jinghai Yang, Changsheng Li, Xue Li, Lili Yang, Yongjun Zhang, Ming Gao, Dandan Wang, Jian Cao, Fabrication and optical properties of Ce-doped ZnO nanorods, *J. Appl. Phys.* 107 (2010) 074302.
- [35] Y.-L. Kuo, C. Lee, Y.-S. Chen, H. Liang, Gadolinia-doped ceria films deposited by RF reactive magnetron sputtering, *Solid State Ionics* 180 (2009) 1421–1428.
- [36] E. Beche, P. Charvin, D. Perarnau, S. Abanades, G. Flamant, Ce 3d XPS investigation of cerium oxides and mixed cerium oxide (Ce<sub>x</sub>Ti<sub>1-x</sub>O<sub>2</sub>), *Surf. Interface Anal.* 40 (2008) 264–267.
- [37] Yu.A. Teterin, A.Yu. Teterin, A.M. Lebedev, I.O. Utkin, The XPS spectra of cerium compounds containing oxygen, *J. Electron Spectrosc. Relat. Phenom.* 88–91 (1998) 275–279.
- [38] F. Larachi, J. Pierre, A. Adnot, A. Bernis, Ce 3d XPS study of composite Ce<sub>x</sub>Mn<sub>1-x</sub>O<sub>2-y</sub> wet oxidation catalysts, *Appl. Surf. Sci.* 195 (2002) 236.
- [39] A. Galtayries, G. Blanco, G.A. Cifredo, D. Finol, J.M. Gatica, J.M. Pintado, et al., XPS analysis and microstructural characterization of a Ce/Tb mixed oxide supported on a lanthana-modified transition alumina, *Surf. Interface Anal.* 27 (1999) 941.
- [40] A. Fujimori, Correlation effects in the electronic structure and photoemission spectra of mixed-valence cerium compounds, *Phys. Rev. B* 28 (1983) 4489.
- [41] P. Burroughs, A. Hamnett, A.F. Orchard, G. Thornton, Satellite structure in the X-ray photoelectron spectra of some binary and mixed oxides of lanthanum and cerium, *JCS Dalton Trans.* (1976) 1686.
- [42] E. Wuilloud, B. Delley, W.D. Schneider, Y. Baer, Spectroscopic evidence for localized and extended f-symmetry states in CeO<sub>2</sub>, *Phys. Rev. Lett.* 53 (1984) 202.
- [43] E. Burstein, Anomalous optical absorption limit in InSb, *Phys. Rev.* 93 (1954) 632.
- [44] Huey-Ing Chen, Hung-Yi Chang, Synthesis of nanocrystalline cerium oxide particles by the precipitation method, *Ceram. Int.* 31 (2005) 795–802.
- [45] C. Aydin, Omar A. Al-Hartomy, A.A. Al-Ghamdi, F. Al-Hazmi, I.S. Yahia, F. El-Tantawy, F. Yakuphanoglu, Controlling of crystal size and optical band gap of CdO nanopowder semiconductors by low and high Fe contents, *J. Electroceram.* 29 (2) (2012) 155–162.
- [46] C.X. Xu, G.P. Zhu, X. Li, Y. Yang, S.T. Tan, X.W. Sun, C. Lincoln, T.A. Smith, Growth and spectral analysis of ZnO nanotubes, *J. Appl. Phys.* 103 (9) (2008) 094303.
- [47] Q.J. Yu, W.Y. Fu, C.L. Yu, H.B. Yang, R.H. Wei, M.H. Li, S.K. Liu, Y.M. Sui, Z.L. Liu, M.X. Yuan, G.T. Zou, G.R. Wang, C.L. Shao, Y.C. Liu, Fabrication and optical properties of large-scale ZnO nanotube bundles via a simple solution route, *J. Phys. Chem. C* 111 (47) (2007) 17521.

- [48] L.F. Xu, Q. Liao, J.P. Zhang, X.C. Ai, D.S. Xu, Single-crystalline ZnO nanotube arrays on conductive glass substrates by selective dissolution of electrodeposited ZnO nanorods, *J. Phys. Chem. C* 111 (12) (2007) 4549.
- [49] Wu. Qingzhi, Xia Chen, Ping Zhang, Yingchao Han, Xiaoming Chen, Yuhua Yan, Shipu Li, Amino acid-assisted synthesis of ZnO hierarchical architectures and their novel photocatalytic activities, *Cryst. Growth Des.* 8 (8) (2008) 3010–3018.
- [50] Gao-Ren Li, Lu. Xi-Hong, Wen-Xia Zhao, Su. Cheng-Yong, Ye-Xiang Tong, Controllable electrochemical synthesis of  $\text{Ce}^{4+}$ -doped ZnO nanostructures from nanotubes to nanorods and nanocages, *Cryst. Growth Des.* 8 (4) (2008) 1276.
- [51] O.M. Ntwaeaborwa, P.H. Holloway, Enhanced photoluminescence of  $\text{Ce}^{3+}$  induced by an energy transfer from ZnO nanoparticles encapsulated in  $\text{SiO}_2$ , *Nanotechnology* 16 (2005) 865.
- [52] Y. Deng, G.S. Wang, N. Li, L. Guo, Synthesis and red-shifted photoluminescence of single crystalline ZnO nanowires, *J. Lumin.* 129 (2009) 55.
- [53] M. Ristic, S. Music, M. Ivanda, S. Popovic, Sol–gel synthesis and characterization of nanocrystalline ZnO powders, *J. Alloys Compd.* 367 (2005) L1.